Strain Rate Effect on the Evolution of Deformation Texture for α-Fe

A. BHATTACHARYYA, D. RITTEL, and G. RAVICHANDRAN

The effect of strain rate on the deformation texture of alpha-iron (α-Fe) is studied at different strain levels during the deformation. Two shear compression specimens (SCS) were deformed in three consecutive stages at room temperature, one at 10^{-3}/s and the other at 10^{+3}/s, to the same strain level. The crystallographic textures were determined using electron backscattered diffraction. The textures at each deformation stage were found to be unaffected by the wide variations in strain rate. By comparing the stress–strain curves and crystallographic texture at the two strain rate levels, it is realized that for α-Fe there is no marked increase in strain hardening at high strain rate with respect to quasi-static tests, so that the deformation texture remains unchanged. The temperature increase that develops at high strain rates is deemed to sharpen the texture.

I. INTRODUCTION

CRYSTALLOGRAPHIC texture, defined as the distribution of orientation of crystals (or grains) in a sample, plays a significant part in the material response and in influencing the anisotropy of macroscopic physical quantities. Knowledge of initial texture has been found to be of particular importance in controlling the "earing" of metal sheets during deep drawing and other sheet-metal forming operations carried out, for example, in the automobile industry.[1–6] Texture studies, in addition to the stress–strain response, also improve our understanding of the underlying crystal plasticity behavior and help in developing crystal-based plasticity models.[7,8,9] So far, researchers have carried out texture analysis as a function of composition,[10,11] strain,[11,12] temperature,[13,14] and moderate strain rates from 10^{-3}/s to 10^{-1}/s.[15,16,17] However, there have been only a few studies done at very high strain rates of the order of 10^3/s.[18,19] Such studies are very much needed to model the material behavior during high rate deformation events such as high-speed machining and ballistic failure, where the texture plays an important role.[20,21] In this article, we have tried to understand the texture evolution as a function of strain rate by performing quasi-static and dynamic deformations to the same strain level, at room temperature. Texture comparisons were made at three different strains by using the same specimens throughout the experiment. In the past, however, independent studies have been conducted at low strain rate of 0.001/seconds[22] and high strain rate of 4500/seconds[23] to understand the texture evolution.

In the present case, analysis is carried out on alpha-iron (α-Fe). The material was deformed at room temperature up to large strains ($\sim$1.4) and over large variations in strain rates (10^{-3}/s to 10^3/s). Texture characterization was done at each intermediate strain level. The role of stacking fault energy (SFE) on texture for FCC metals has already been documented,[24,25] and therefore it is expected that the material strain hardening would play a similar role in controlling the textures at various strain rates. Thus, the texture results are analyzed with respect to the corresponding mechanical response, and an explanation is provided for the textural behavior based on dislocation theory.

It has always been an engineering challenge to design a single sample type that can be used over a wide range of strains and strain rates. Recently, Rittel *et al*. developed a unique sample geometry that could be used throughout to achieve large deformations uniformly over wide strain rates.[26,27] This new specimen is known as shear compression specimen (SCS) and is shown schematically in Figure 1. Two equal slots are machined on either side of the specimen at 45 degrees to the loading axis for maximum shear in the gage region. Under normal compression, the gage section experiences a shear dominant deformation, while the bulk of the specimen remains undeformed. Large strains of the order of 1.0 to 1.5 can be achieved with the proper choice of gage dimensions. Similarly, strain rates ranging from 10^{-4}/s (quasi-static) to 10^{+4}/s (dynamic) can also be easily reached. The validation of such a specimen has already been carried out on OFHC Cu,[27] 1018 cold-rolled steel,[28] and a tungsten heavy alloy[29] by comparing the SCS results with the solid cylindrical specimen under compression. A detailed numerical characterization of the SCS can be found in Dorogy and Rittel.[30,31] In this article we use the SCS for carrying out a study on α-Fe. The mechanical response from such a specimen can then be easily compared with the data already available in the literature from cylindrical specimens under compression. Also, SCS is a convenient sample for carrying out large shear dominant deformation at large strain rates $\sim 10^3$/s to 10^4/s.

The article is organized as follows: first, the basic aspects of the SCS with some modifications for the present case are outlined in Section II. The experimental details are mentioned in the second part of Section II. The texture results, along with the stress–strain response from the high rate and quasi-static tests, are laid in Section III. Section IV carries the discussion part, where the texture results from the SCS are compared with the known torsion results (at low strain rate) and correlation is drawn between texture and strain hardening. This section is followed by concluding remarks.

A. BHATTACHARYYA, Postdoctoral Student, and G. RAVICHANDRAN, Professor, are with the Graduate Aeronautics Laboratories, Aeronautics and Mechanical Engineering, California Institute of Technology, Pasadena, CA, U.S.A. Contact e-mail: ab03@caltech.edu D. RITTEL, Faculty Member, is with Mechanical Engineering, Technion, Haifa, Israel.

Manuscript submitted August 3, 2005.

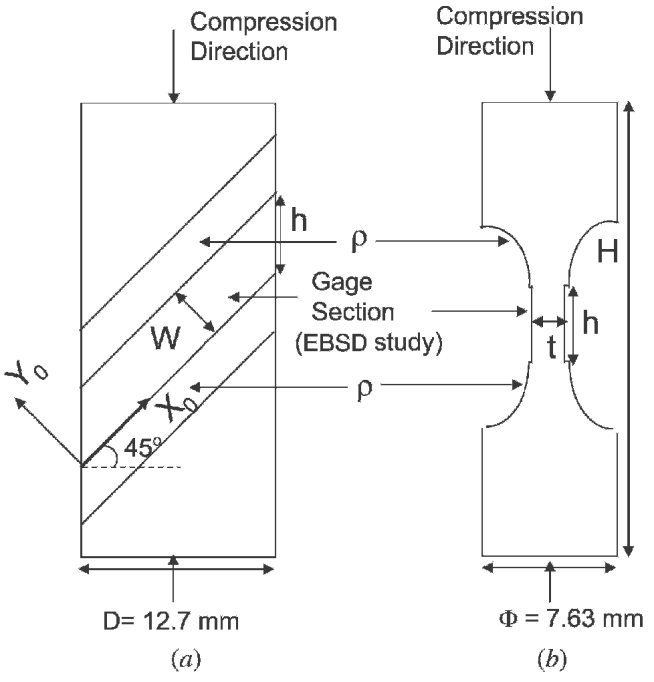

Fig. 1—Schematic of the two cross-sections of the SCS specimen showing (*a*) the gage width (W) and (*b*) the gage thickness (t). The EBSD measurements were made on the outer surfaces of the gage section. The sample height (H), width (D), breadth (Φ), clearance (ρ = 3.3 mm), and initial gage dimensions were same for the two specimens studied in this case, one deformed quasi-statically in the MTS and the other deformed dynamically in the split-Hopkinson bar.

II. EXPERIMENTAL PROCEDURES

A. *Specimens and Testing*

Two rectangular α-Fe samples were cut from the same material batch and selected for carrying out compression tests at widely different strain rates. These samples were made into SCS by machining two equal slots at 45 degrees on either side along the height (*i.e.*, the compression direction) of the sample (Figure 1). The initial height (H) was 20 mm, the gage width (w) was 2.60 mm, and the gage thickness (t) was 2.35 mm, same for both the specimens.

Specimen 1 was compressed quasi-statically, under displacement control, at strain rates of the order of 10^{-3}/s using a computer-controlled servo-hydraulic machine (MTS Model No. 11,019). The test involved placing the specimen in a compression fixture made of hardened steel with the compression rods being perfectly aligned so as to minimize any shear forces at the loading rod–sample interface. The fixture (along with the sample) was in turn placed between the platens of the MTS machine. The load-displacement data obtained from the crosshead movement were later corrected by taking into account the machine and the fixture compliance.

Specimen 2 was compressed dynamically at strain rates of the order of 10^{+3}/s using the split-Hopkinson (Kolsky) pressure bar apparatus. The bars were made of precision-ground high-strength C350 maraging steel. The bars had a common diameter of 19.05 mm, with the incident bar being 59.5 cm long and the transmitted bar being 62.1 cm long. The technique has been well established for high strain rate tests.[32]

The experiment involved compressing the two SCS's to the same strain at these two widely different strain rates. The compression was carried out in three stages, with the height of the sample (H) being reduced by 9 pct, 7 pct, and 9 pct successively. To control the amount of compression of specimen 2 dynamically in the Kolsky bar, a stop-ring made of high-strength C350 maraging steel was placed on the transmitted bar of the split-Hopkinson pressure bar surrounding the specimen. After the impact, the specimen was compressed to a height that was governed by the length of the stop-ring (undergoing minimal deformation). Therefore, the stop-ring length was made such that would result in the reduction of the height of specimen 2 to the same level as that of the quasi-statically compressed specimen 1. For further controlled dynamic compressions of specimen 2, the height of the stop-ring was remachined each time to the desired requirement.

Crystallographic orientation measurements were carried out on the outer surfaces of the gage section (Figure 1). The determination was done by using an HKL Technology Channel 5 software, which employs fully automated (computerized) identification of the electron backscattered diffraction (EBSD) patterns and an automated computation of the crystal lattice orientation. For proper detection and recording of the diffraction patterns from the gage section in the SEM chamber, a clearance (ρ) was made along the sides of the notched section (Figure 1). This also helped in electropolishing the gage section every time after the deformation for better EBSD results. The gage section was initially characterized before any deformation. The undeformed crystallographic texture in the gage section was observed to be random for both the test specimens. Such random textures were also observed at the top and bottom flat surfaces of the specimen. In addition, the average initial grain size was found to be around 75 μm. The initial microstructure in the gage section is shown schematically in Figure 2, which is representative of the two specimens studied here. Successive EBSD measurements were carried out in the gage section after every compression, for both the specimens.

B. *Data Reduction*

When the SCS is compressed, the gage section actually experiences a three-dimensional state of stress with the dominance of shear stress. From the past computational analysis done on the SCS by Rittel *et al.*,[27,28] the stresses and strains in the gage section are reduced to the equivalent von Mises stress (σ_e), strain (ε_e), and strain rate ($\dot{\varepsilon}_e$). The constitutive relations for the SCS are given by

$$\varepsilon_e = K_3 \frac{d}{h} : \dot{\varepsilon}_e = K_3 \frac{\dot{d}}{h} \qquad [1]$$

$$\sigma_e = K_1(1 - K_2\varepsilon_e) \frac{P}{Dt} \qquad [2]$$

where d = the vertical displacement of the gage section, h = the initial gage height, P = the applied load, and D and t = the sample width and gage thickness shown in Figure 1. The parameters K_1, K_2, and K_3 were found to be functions of the gage width and the material. By comparing the SCS load-displacement data for α-Fe with the corresponding data available from the cylindrical samples, K_1, K_2, and K_3 were taken as 1.0, 0.05, and 1.0, respectively.

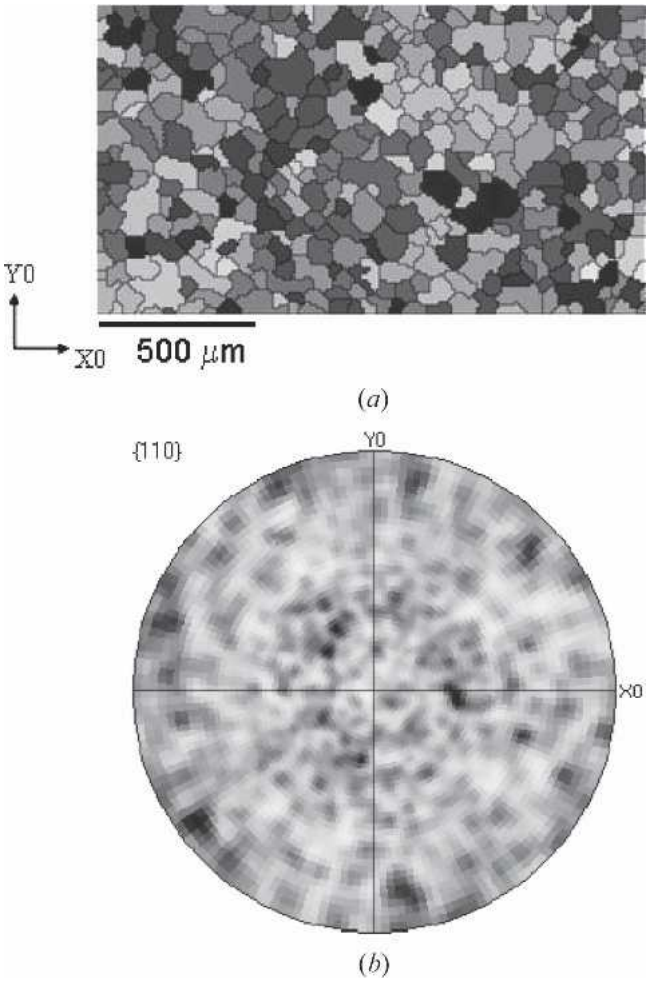

Fig. 2—Initial microstructure of bcc Fe, which is representative of specimens 1 and 2, showing (*a*) an average grain size of 75 μm and (*b*) a random texture.

III. RESULTS

A. *Quasi-Static Deformation*

1. *Mechanical response*

Figure 3(a) shows the stress–strain curves of specimen 1 under quasi-static deformation during loading/reloading during the three stages of compression. Apart from a slight increase in the flow stress after every reloading, the material exhibits a marked upper and lower yield point. These features are typically observed in iron and steel due to the presence of interstitial impurities and strain aging mechanisms.

2. *Deformed grain structure*

Figure 4(a) shows the micrograph of the deformed grains in the gage region after the final deformation. The sample was chemically etched using a solution of 5 mL nitric acid and 95 mL ethanol to reveal the grain structure. The grains appear compressed and sheared after the deformation.

3. *Crystallographic texture analysis*

Figure 5(a) shows the evolution of texture in the gage section with strain starting from the initial random texture. The axes were chosen (shown in Figure 1) in such a way that the $(+x_0)$ axis is along the negative shear in the gage section. At large strains, the texture resembles the known torsion texture

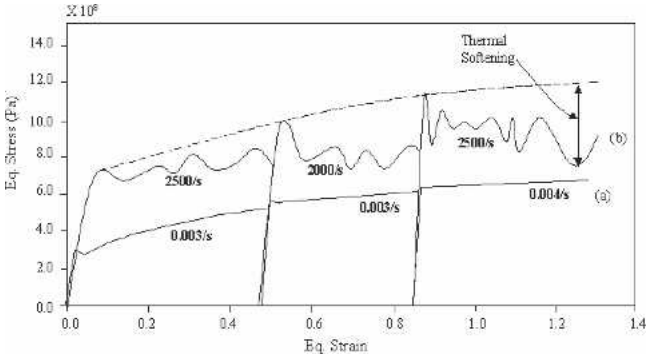

Fig. 3—Stress–strain response of SCS α-Fe under (*a*) quasi-static (specimen 1) and (*b*) dynamic (specimen 2) loading. Also shown are the actual strain rates during the deformation. Although the sample (H) was compressed by 9 pct, 7 pct, and 9 pct successively, the equivalent strain (ε_e) in the gage section was around 0.5, 0.9, and 1.4, based on Eq. [1]. The dotted line is drawn by joining the yield points for the high rate tests.

for α-Fe[33,34] as the deformation in the gage section is shear dominated. With the increase in shear strain, it is also carefully noticed that the texture rotates counter-clockwise about the normal axis (out of the plane of the paper). This feature has also been reported by other researchers for α-Fe under torsion tests.[33,34]

B. *Dynamic Deformation*

1. *Mechanical response*

Figure 3(b) similarly shows the stress–strain response of specimen 2 during the dynamic deformation. The flow stress increases considerably with the increase in strain rate, a feature more prominent in bcc metals as opposed to FCC metals. We also observe that at larger strains there is lowering of strain hardening turning eventually into strain softening. This is probably due to the adiabatic heating in the gage section during dynamic deformation, which is commonly noted in other dynamic room-temperature tests.

2. *Deformed grain structure*

Figures 4(b) and (c) show the micrograph of the deformed grains after the final deformation. There is no observation of recrystallized grains during the dynamic deformation after a strain of 1.4.

3. *Crystallographic texture analysis*

Figure 5(b) shows the evolution of texture in the gage section with strain starting from the initial random texture. By comparing it with the corresponding texture results under quasi-static deformation shown in Figure 4(a), we observe a striking similarity in the deformation textures at intermediate strain levels (Figures 5(a1) and (a2) with Figures 5(b1) and (b2), respectively), for a difference in the strain rate of the order of 10^6/s. The texture seems to be independent of the strain rate.

To analyze the results, some important ideal orientations observed during torsion are reported in Table I along with their location in (110) pole figure, shown in Figure 6.[34]

For an accurate comparison of the texture results, the orientation distribution functions (ODFs) have been plotted. Figures 7 and 8 show the corresponding ODFs for the low strain rate and the high strain rate tests, respectively.

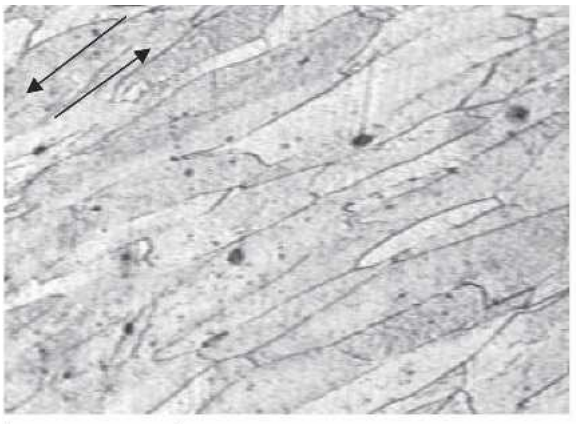

(*a*)

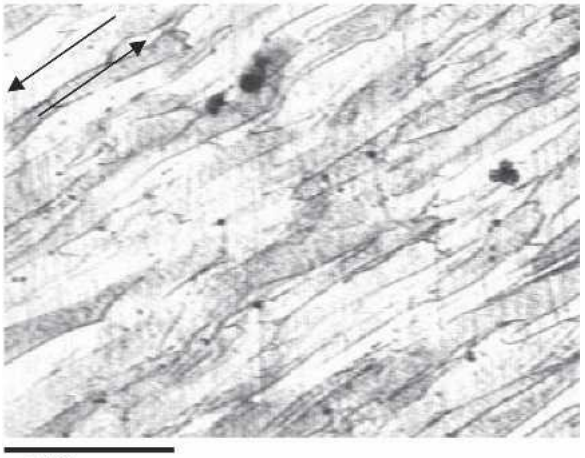

(*b*)

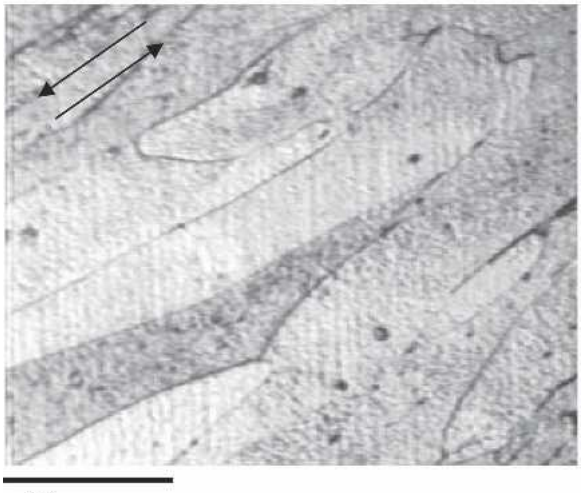

(*c*)

Fig. 4—Micrograph showing the deformed grains in the gage section after a strain of 1.4 in specimen 1 under quasi-static deformation (200 times magnification) (*a*) and specimen 2 under dynamic deformation at two different magnifications, (*b*) 200 times magnification and (*c*) 600 times magnification. There is no evidence of dynamic recrystallization at the high strain rates. Also indicated is the direction of shear.

Qualitatively, the ODF maps at intermediate strain levels are very similar to each other (Figures 7(a1) and 8(b1), and Figures 7(a2) and 8(b2)). Quantitatively, at a strain of ~0.5, during the quasi-static test (Figure 7(a1)) the J1 and J2 components are the most intense (~8.0), followed by F ~4.0, whereas at high strain rate (Figure 8(b1)) the intensity is the highest near the J2 component (~8.0), followed by J1 and F ~4.0. The intensity of J2 is ~4.0 in Figure 8(b1), which makes the intensity ratio of J1/J2 to be nearly constant (~1.0) for both the cases. The E2 component appears a bit stronger at high strain rate than that at low strain rate. The intensities of other components, D1, D2, and E1, are nearly the same in both the tests.

As the strain is increased to 0.9, all the texture components are of nearly the same intensity at these two widely different strain rates.

Finally, at the strain of 1.4, we observe that at high strain rate (Figure 8(b3)), on one hand the F component disappears (~0.0), but on the other hand, the intensity of the other components, J1, J2, D1, D2, and E1, becomes considerably stronger that those at low strain rate. However, the intensity ratios, J1/J2 and D1/D2, are nearly the same in both the tests.

Additional comparison is provided by plotting a histogram of the volume fraction of these ideal orientations (Figure 9). The fractions are computed for a deviation of 10 degrees from their ideal orientation. Firstly, as expected, there is an increase in the volume fraction of these components from their initial values, after a strain of 0.9, during quasi-static and dynamic tests. Secondly, the ideal texture components at these two widely different strain rates have nearly the same volume fraction (within the uncertainty) after a strain of 0.9. Eventually, after the final strain of ~1.4, we observe strong contribution from J1 (in particular) and J2 components at high strain rate. There is also an increase in the intensity of other components, excepting F ((110) [001]), which disappears at the high rate. Such difference in the texture intensities is revealed in the (110) pole figure, where the orientation density is more concentrated at the edges than around the central region of the pole figure at high strain rate (comparison between Figures 5(b3) and (a3)). Apart from this distinction at the final strain level, the most important feature that we find here is that the *texture at high strain rate looks very similar to the texture at quasi-static strain rates*, starting with the same initial random texture, when compared at the same strain level, at low and intermediate strains (<1.0). This observation clearly indicates that the deformation texture is independent of the strain rate, from 10^{-3}/s to 10^{+3}/s, for bcc Fe. Similar observations have also been reported earlier. Matsuoka *et al.*[35] analyzed the effect of strain rate (10^2/s to 10^3/s) during hot rolling of iron and observed no change in the texture type when compared with the cold-rolled texture, and Oesterle[36] observed no change in texture while studying the effect of temperature during rolling of iron. However, unlike our present study, none of the earlier work was geared toward understanding the reason behind this similarity.

C. *Uniformity of Deformation*

To check the uniformity of the texture results, EBSD scans were performed at random places along the midsection on either side of the gage region. It was found that the texture remained unchanged, which indicates that the deformation was uniform in the SCS gage section. A numerical validation of this particular feature has been reported by Rittel *et al.*[26,27]

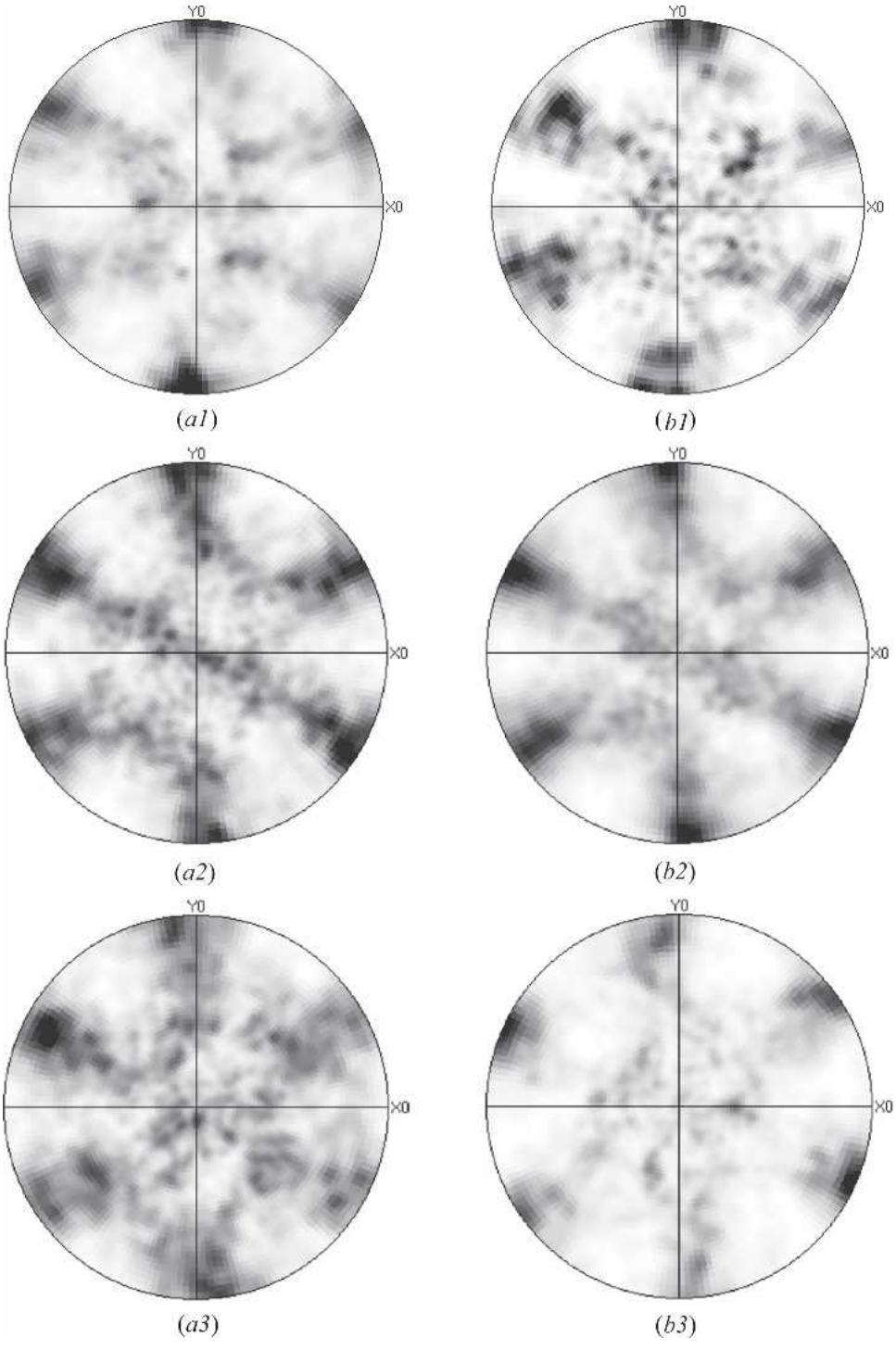

Fig. 5—(110) pole figure of the deformed SCS α-Fe in the gage section plotted in the X_o-Y_o frame (Figure 1), with (*a1*), (*a2*), and (*a3*) showing the quasi-static texture (specimen 1) and (*b1*), (*b2*), and (*b3*) showing the dynamic texture (specimen 2). 1, 2, and 3 represent the three successive compression stages of the SCS.

D. *Texture Studies in the Underformed Region*

During the deformation, texture measurements were also carried out at the top and bottom flat surfaces of the specimens. As expected, there was no change in the texture with respect to its initial texture—*i.e.*, the texture remained "random" during the deformation, for both the specimens, indicating that deformation was fully restricted in the gage region.

IV. DISCUSSION

To understand the textural similarity at these two widely different strain rates, the corresponding mechanical response is looked at for analysis. The high strain rate stress–strain curve exhibits higher yield strength than the quasi-static one after every loading, and interestingly the difference between the two remains nearly constant. In other words, the initial difference in the yield stress is around the same when computed

Table I. Euler Angles of Important Ideal Orientations Under Torsion of α-Fe

Orientation	Phi1 (ϕ1)	Phi (Φ)	Phi2 (ϕ2)
D1	125.3	45.0	0.0
D2	54.7	45.0	0.0
E1	39.2	65.9	26.6
E2	90.0	35.3	45.0
F	180.0	45.0	0.0
J1	30.0	54.7	45.0
J2	90.0	54.7	45.0

The location of these orientations in (110) pole figure is shown in Figure 6.[34]

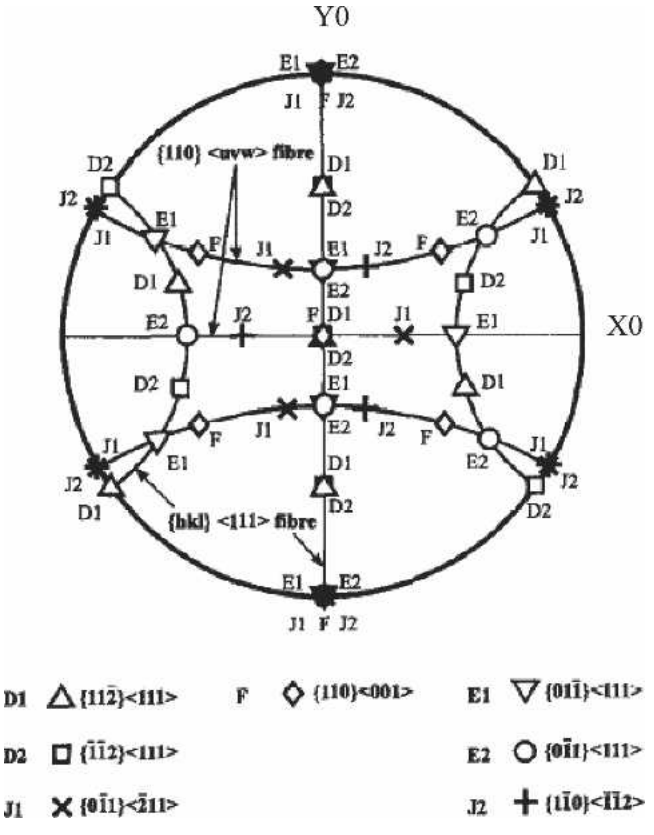

Fig. 6—The (110) pole figure showing the ideal orientations observed during torsion for bcc Fe.[34]

at the strains of 0.45 and 0.9 and is ~450 MPa. This aspect further leads to the consideration that if the deformations at high strain rates were carried out incrementally (*i.e.*, small increase in strain), then the resulting strain hardening curve plotted by connecting the yield points would look very similar to the corresponding curve under quasi-static deformation. Such a curve is plotted by the dotted line in Figure 3(b). We can therefore surmise that strain hardening is independent of strain rate, in the studied range, if the thermal softening is neglected at high strain rates, for bcc Fe, as is observed in general for bcc metals at quasi-static strain rates from 10^{-6}/s to 1.0/s.[37]

The effect of the strain hardening on texture is realized when we also notice that the texture remains unchanged with the strain rate for α-Fe. It is important to mention here that Bhattacharyya *et al.*[38] performed similar texture comparisons for OFHC Cu after a single hit (*i.e.*, single deformation stage). It was found that the texture at high rate was different than the texture at quasi-static strain rate, and from the stress–strain curves it was observed that the high strain rate deformation test had a higher *initial* strain hardening than the quasi-statically deformed test.

Therefore, from these two experimental observations we have found a direct one-to-one correlation between the strain hardening and the deformation texture. An increase in strain hardening at high strain rate modifies its texture corresponding to its low rate result, whereas a similarity in hardening results in the similarity in textures.

One can estimate the temperature rise (ΔT) in the gage section during the dynamic deformation by considering that a significant part of the mechanical work gets converted into heat

$$\Delta T = \frac{\beta}{\rho C_p} \int_0^{\varepsilon} \sigma_e \, de_e \qquad [3]$$

where β = the fraction of the plastic work converted into heat, σ_e and e_e = the equivalent stresses and strains, and ρ and C_p = the density and specific heat capacity, respectively. In the case of α-Fe, ρ = 7874 kg/m^3 and C_p = 452 J/kg K. Assuming β = 0.9, ΔT is estimated from Figure 3(b) to be 75 K during the first deformation stage, 79 K during the second deformation stage, and 101 K during the third deformation stage. In the present experiments, adiabatic heating effects were necessarily limited as a result of the interrupted nature of the tests. However, we note that the effect of dynamic recovery is more prominent during the third stage (or the final stage) of deformation, which thereby results in the sharpness of its deformation texture compared to the corresponding quasi-static case. Similar results have also been reported by Lee *et al.* on bcc Ta[18] when tested with cylindrical specimens.

To understand the extent to which texture is being controlled by strain hardening, we base our analysis on the dislocation theory. It is known that strain hardening is primarily governed by dislocation–dislocation interaction—*i.e.*, higher strain hardening indicates that larger stresses are needed to free the dislocations from its entanglements. As the dislocations glide toward the grain boundary and become accumulated, an increased misorientation between the adjacent grains results that contributes to an observed grain rotation. At high strain rates, the stress needed for the initiation of dislocation motion increases, resulting in higher yield strength. For bcc metals, at room temperature and under quasi-static deformation, the material exhibits very low strain hardening due to the ease with which the dislocations can cross-slip and overcome obstacles. There are 48 possible slip systems for bcc metal, and therefore it has a low strain hardening coefficient (n), which is given by $d(\ln \sigma_e)/d(\ln \varepsilon_e)$. In our present experiment, n is ~0.25 at quasi-static strain rate, which is close to the reported value in the literature.[39] Consequently, changes in strain rates (or temperature) have less effect on n, thereby resulting in similar hardening even when the strain rate is increased by a factor of six decades. Since the dislocation network is unaffected at high strain rate, so are the grain rotation and texture. In the case of FCC metal, the propensity for cross-slip is directly related to stacking fault energy (SFE), which is a strong function of temperature (and hence also a function of the strain rate). Cu

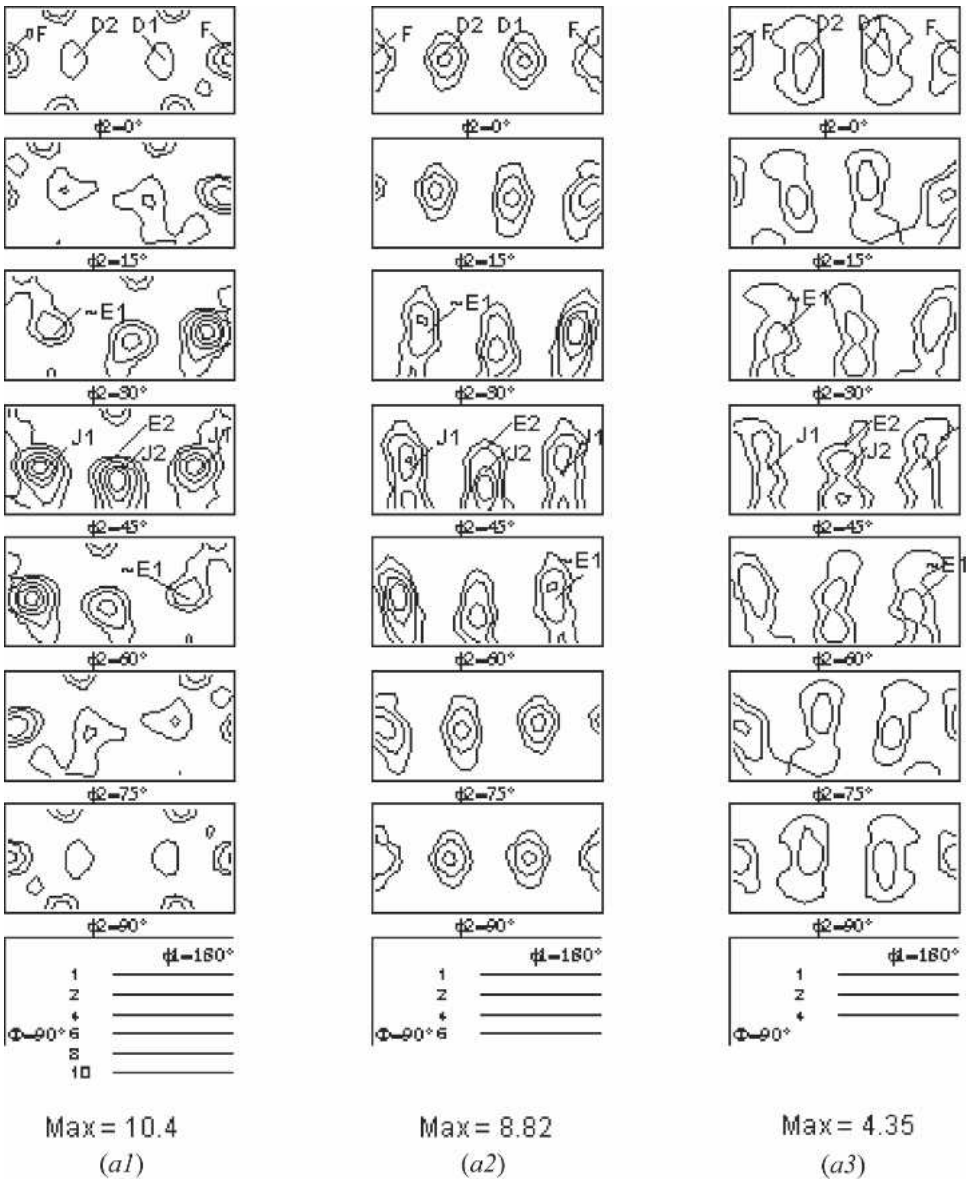

Fig. 7—Orientation distribution function (ODF) of the quasi-static deformation textures (Figures 5(*a1*), (*a2*), and (*a3*)) developed during the three successive compression stages of the SCS. The location of ideal orientations based on Table I is indicated in the ODFs.

has low SFE at room temperatures and therefore has a moderately high n of ~0.50[39] (in addition to the fact that the number of possible slip systems is 12), which is enhanced at higher strain rate. Correspondingly, the grain rotation is adversely affected due to the lack of dislocation motion across obstacles, leading to the textures being different at different rates.

Thus, deformation texture is influenced by strain hardening rate. The similarity in texture observed for α-Fe is expected to be independent of the mode of deformation (*i.e.*, not just restricted to shear, as in this case).

The temperature increase at high strain rate results in dislocation annihilation, thereby causing strain softening. Also, the grain boundaries that had a gradual variation in orientation (due to the high density of dislocations at the grain boundary) become sharper due to dislocation annihilation. This leads to the appearance of a sharper pole figure (Figure 5(b3)) due to the strong enhancement of particular texture components such as J1 and J2 (Figures 8(b3) and 9). This reorientation also leads to disappearance of other components such as F. We believe that the temperature rise during each dynamic test is in the recovery region and is below the temperature needed for dynamic recrystallization (~600 °C).[40] For further validation of this aspect in the current study, a misorientation profile is plotted between the neighboring points after the final deformation for both the quasi-static and the dynamic case (Figure 10). We can readily see that at higher strain rate the low-angle grain boundaries (selected arbitrarily as 15 degrees) disappear and there is a corresponding increase in high-angle grain boundaries due to the thermal softening. This effect is similar to the conventional dynamic softening (or recovery). Sharper textures were also noticed by Lee *et al.*[18] at high strain rates for Ta.

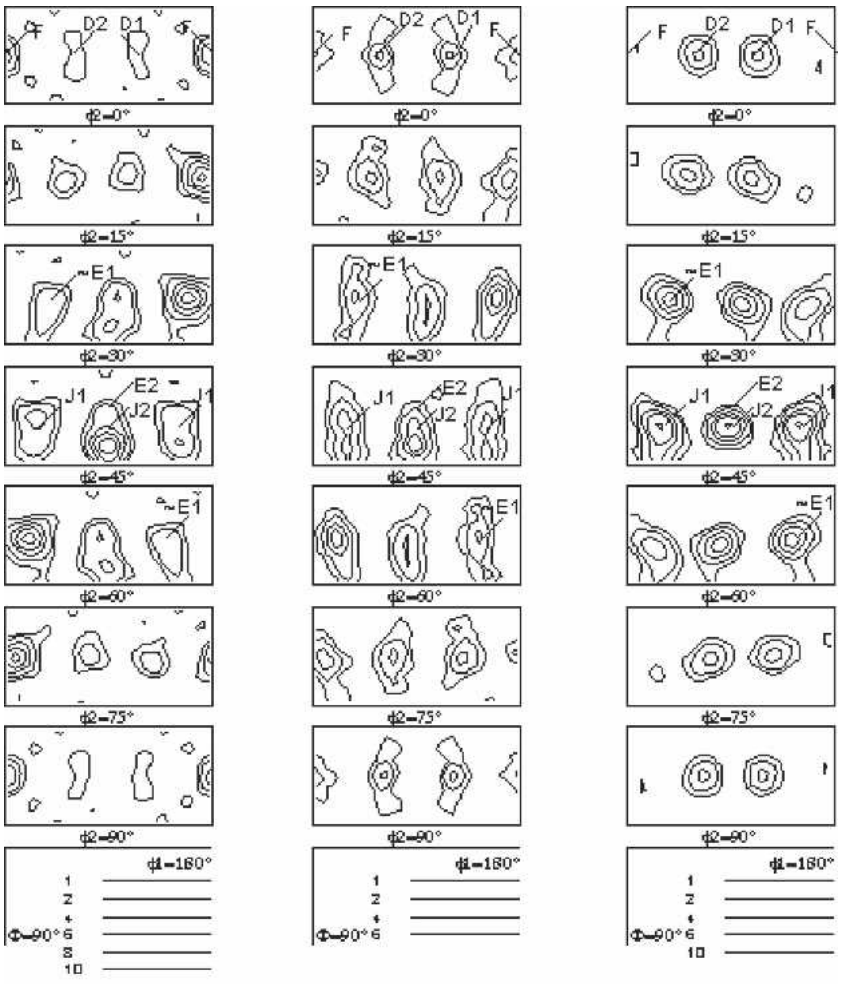

Fig. 8—Orientation distribution function (ODF) of the dynamic deformation textures (Figures 5(*b1*), (*b2*), and (*b3*)) developed during the three successive compression stages of the SCS. The location of ideal orientations based on Table I is indicated in the ODFs.

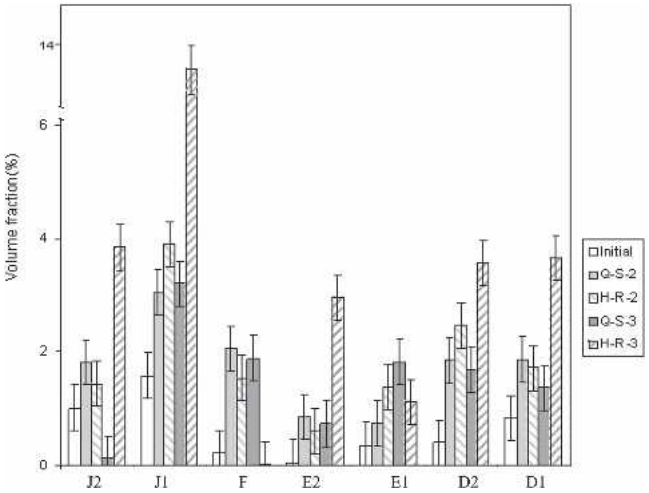

Fig. 9—Volume fractions (pct) of the ideal orientations mentioned in Table I under quasi-static (Q-S) and high strain rate deformation (H-R) at various strains. 2 and 3 refer to strain of 0.5 and 1.4, respectively. "Initial" refers to the undeformed state. The values are computed for a variation of 10 degrees from their respective orientations.

V. CONCLUSIONS

The effect of strain rate, up to (10^{+3}/s), on deformation texture of α-Fe has been investigated at room temperature by means of EBSD. For this range of strain rates, the following conclusions can be drawn from this study:

1. There is no observable change in texture at low and intermediate strains (<1.0) when the strain rate is increased from quasi-static level (10^{-3}/s) to dynamic level (10^{+3}/s).
2. At large strains (>1.0), the texture appears sharper for the high strain rate deformed sample *vs* the low strain rate deformed sample.
3. A direct correspondence is found between the strain hardening rate and deformation texture. Material with a high initial strain hardening exponent ($n \sim 0.5$) increases with strain rate; this restricts the grain rotation, which therefore affects the texture. Alternately, material with a low strain hardening exponent has no significant increase in strain hardening, thereby causing no observable change in texture. Pending further investigation, strain rate has little effect on texture for bcc Fe.

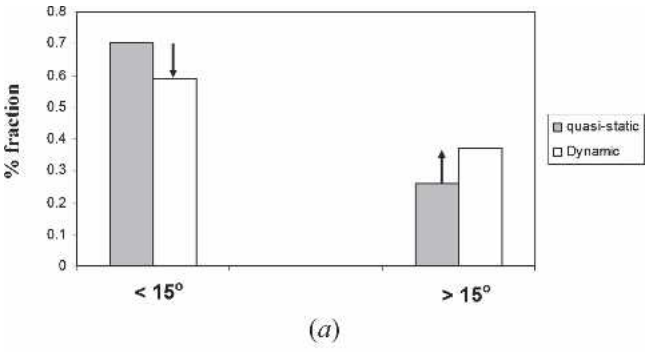

(*a*)

(*b*)

Fig. 10—(*a*) The misorientation angle between neighboring pixel points for the quasi-statically deformed sample (specimen 1) and the dynamically deformed sample (specimen 2). The low-angle grain boundaries (<15 degrees) for the dynamically deformed sample are converted into high-angle grain boundaries during thermal softening. (*b*) A representation of image quality map in the gage section after the final deformation. Out of 21,000 pixel points interrogated, 36 pct were indexed as bcc Fe.

4. The moderate temperature rise during the dynamic tests (*i.e.*, dynamic recovery) seems to sharpen the texture.

ACKNOWLEDGMENTS

The support of the Department of Energy through the Center for Dynamic Response of Materials at the California Institute of Technology is gratefully acknowledged. D.R. acknowledges the Fund for Promotion of research at Technion.

REFERENCES

1. T.L. Richards: *Prog. Metal Phys*., 1949, vol. 1, pp. 281-305.
2. J.C. Wright: *J. Inst. Metals*, 1965, vol. 93, pp. 289-97.
3. G.E.G. Tucker: *Acta Metall*., 1961, vol. 9, pp. 275-86.
4. J. Hirsch, R. Musik, and K. Lucke: *Proceedings of the Fifth International Conference on Texture of Materials*, G. Gottstein and K. Lucke, eds., Springer-Verlag, Berlin, 1978, p. 437.
5. H. Sumitomo and H. Yoshimura: *Proceedings of the Seventh International Conference on Texture of Materials*, C.M. Brakman, P. Jogenberger, and E.J. Mittemeijer, eds., Netherlands Society for Material Science, Zwijindrecht, 1984.
6. H. Inagaki: *Z. Metallkd*., 1991, vol. 82, pp. 361-72.
7. R. Asaro and A. Needleman: *Acta Metall*., 1985, vol. 33, pp. 923-53.
8. S. Kalidindi, C. Bronkhorst, and L. Anand: *J. Mech. Phys. Solids*, 1992, vol. 40, pp. 537-69.
9. K. Mathur and P. Dawson: *Int. J. Plast*., 1989, vol. 5, pp. 67-94.
10. M. Koizumi, S. Kohara, and H. Inagaki: *Z. Metallkd*., 2000, vol. 91, pp. 88-96.
11. J. Hirsch and K. Lücke: *Acta Metall*., 1988, vol. 36, pp. 2863-82.
12. I.L. Dillamore and W.T. Roberts: *Acta Metall*., 1964, vol. 12, pp. 281-93.
13. H. Hu and R.S. Cline: *J. Appl. Phys*., 1961, vol. 32, pp. 760-63.
14. H. Hu and S.R. Goodman: *Trans. Metall. Soc. AIME*, 1963, vol. 227, pp. 627-39.
15. M.T. Perez-Prado, M.C. Cristina, M. Torralba, O.A. Ruano, and G. Gonzalez-Doncel: *Scripta Mat*., 1996, vol. 35, p. 1455.
16. C.I. Maurice and J.H. Driver: *Mater. Sci. Forum*, 1996, vol. 217, pp. 547-52.
17. N. Stanford, D. Dunne, and M. Ferry: *Acta Mater*., 2003, vol. 51, pp. 665-76.
18. B.J. Lee, K.S. Vecchio, S. Ahzi, and S.E. Schoenfeld: *Metall. Mater. Trans*., 1997, vol. 28A, pp. 113-22.
19. J.W. House and P.P. Gillis: *Mater. Sci. Forum*, 2002, vol. 408, pp. 547-51.
20. B.K. Kad, S.E. Schoenfeld, and M.S. Burkins: *Mater. Sci. Eng. A*, 2002, vol. 322, pp. 241-51.
21. H. Hu, A. Zarkades, and F.R. Larson: *Texture of Crystalline Solids*, 1980, vol. 4, pp. 73-92.
22. S.R. Kalidindi, A. Bhattacharyya, and R.D. Doherty: *Proc. R. Soc. London A*, 2004, vol. 460, pp. 1935-56.
23. D.W. Brown, S.P. Abeln, W.R. Blumenthal, M.A.M. Bourke, M.C. Mataya, and C.N. Tome: *Metall. Mater. Trans*., 2005, vol. 36A, pp. 929-39.
24. H. Suwas, L.S. Toth, J.J. Fundenberger, T. Grosdidier, and W. Strotzki: *Solid State Phenomena*, 2005, vol. 105, pp. 345-50.
25. D.A. Hughes, R.A. Lebensohn, H.R. Wenk, and A. Kumar: *Proc. R. Soc. Lond. A*, 2000, vol. 456, pp. 921-53.
26. D. Rittel, S. Lee, and G. Ravichandran: *Exper. Mech*., 2002, vol. 42, pp. 58-64.
27. D. Rittel, G. Ravichandran, and S. Lee: *Mech. Mater*., 2002, vol. 34, pp. 627-42.
28. M. Vural, D. Rittel, and G. Ravichandran: *Metall. Mater. Trans. A*, 2003, vol. 34A, pp. 2873-85.
29. D. Rittel, R. Levin, and A. Dorogoy: *Metall. Mater. Trans. A*, 2004, vol. 35A, pp. 3787-95.
30. A. Dorogoy and D. Rittel: *Exper. Mech*., 2005, vol. 45, pp. 167-77.
31. A. Dorogoy and D. Rittel: *Exper. Mech*, 2005, vol. 45, pp. 178-85.
32. G.T. Gray, III: *ASM Handbook*, 2000, vol. 8, p. 462.
33. F. Montheillet, M. Cohen, and J.J. Jonas: *Acta Mater*., 1984, vol. 32, pp. 2077-89.
34. J. Baczynski and J.J. Jonas: *Acta Mater*., 1996, vol. 44, pp. 4273-88.
35. S. Matsuoka, K. Sakata, S. Satoh, and Y. Kato: *ISIJ Int*., 1994, vol. 34, pp. 77-84.
36. W. Oesterle: *Netherlands Soc. Mater. Sci*., 1984, pp. 123-28.
37. A.S. Khan and R.Q. Liang: *Int. J. Plast*., 1999, vol. 15, pp. 1089-109.
38. A. Bhattacharyya, D. Rittel, and G. Ravichandran: *Scripta Mater*., 2005, vol. 52, pp. 657-61.
39. *ASM Handbook Mechanical Testing and Evaluation*, 2000, vol. 8, p. 71.
40. J. Baczynski and J.J. Jonas: *Metall. Mater. Trans. A*, 1998, vol. 29A, pp. 447-62.